PROCEEDINGS OF SPIE

SPIEDigitalLibrary.org/conference-proceedings-of-spie

Design and development of novel rotary actuation system based on shape memory alloy springs driven mechanism arranged in bipennate muscle architecture

Yashaswi Sinha, Kanhaiya Lal Chaurasiya, Yash Ashok Kumar Patel, Tanuj Gupta, Bishakh Bhattacharya

Yashaswi Sinha, Kanhaiya Lal Chaurasiya, Yash Ashok Kumar Patel, Tanuj Gupta, Bishakh Bhattacharya, "Design and development of novel rotary actuation system based on shape memory alloy springs driven mechanism arranged in bipennate muscle architecture," Proc. SPIE 12483, Active and Passive Smart Structures and Integrated Systems XVII, 124831K (28 April 2023); doi: 10.1117/12.2658471

SPIE.

Event: SPIE Smart Structures + Nondestructive Evaluation, 2023, Long Beach, California, United States

Design and development of novel rotary actuation system based on shape memory alloy springs driven mechanism arranged in bipennate muscle architecture

Yashaswi Sinha[a], Kanhaiya Lal Chaurasiya[a], Yash Ashok Kumar Patel[b], Tanuj Gupta[a], and Bishakh Bhattacharya[a]

[a]Indian Institute of Technology Kanpur, Uttar Pradesh, India
[b]National Institute of Technology Tiruchirappalli, Tamil Nadu, India

ABSTRACT

Actuators regulate motion in manufacturing and industrial automation by applying an excitation force or torque. Conventional actuators do have their advantages; however, they have multiple components (prone to wear and tear), are expensive during maintenance, bulky, and suffer from backlashes. Therefore, smart-material-based actuators have been increasingly proposed to overcome such shortcomings. Shape memory alloy (SMA) is generally considered for such applications due to its high power-to-weight ratio, noise-free, energy-efficient operation, and facilitating miniaturization. The current research exploits the advantages of the pennate musculature with the properties of SMA to develop a bipennate SMA-based rotary actuator. Pennate muscle fibers are aligned obliquely to the muscle line of action, enabling fiber force to be coupled to macro-level muscle force, resulting in increased force output. The study presents an ergonomic-design-integration-framework of an SMA-driven rotary actuator. The lightweight gearless actuator has drivability without backlash, compatible with a rhombus-based-compliant power transmission system. An analytical model of the bipennate SMA-based rotary actuator has been developed and experimentally validated. The new actuator delivers at least twice the actuation torque (2.1 N-m) compared to the SMA-based rotary actuators reported in the literature. The actuator also delivers a high associated angular displacement ranging from 60°-70°. The actuator design parameters have been optimized by implementing a constrained gradient descent algorithm such that the output torque, stroke, and efficiency of the actuator system can be tailored as per the requirement and application. The actuator has varied applications, from healthcare devices to next-generation space robots.

Keywords: Bipennate muscle, Shape memory alloy, Rotary actuator, Additive manufacturing, SMA spring analytical model

1. INTRODUCTION

Biological organisms, such as mammals, have various types of muscle architecture present, with each serving a particular purpose. Nevertheless, most muscle architecture can generally be classified under two vast categories, parallel and pennate. While parallel architecture is generally found in places where a high strain is required, on the other hand, pennate architecture can accommodate a larger number of muscle fibers in a given physiological area, and thus a higher amount of force can be generated. In the current study, the shape memory alloy (SMA) spring is arranged in a bipennate configuration analogous to the extensor side of the thigh *quadriceps femoris*.[1,2] The bipennate configuration of SMA wire has been used previously to develop a high-force linear actuator, where six bipennate units of SMA wires were able to develop a force of greater than 100 N.[3]

Actuators, on the other hand, are quite important to systems owing to their varied applications. Conventional actuators do have their advantages; however, they have multiple components (prone to wear and tear), are expensive during maintenance, bulky, and suffer from backlashes. The electromagnetism-based driving principle

Further author information: (Send correspondence to B.B.)
Y.S.: E-mail: ysinha@iitk.ac.in
K.L.C.: E-mail: kanhaiya@iitk.ac.in
B.B.: E-mail: bishakh@iitk.ac.in

Active and Passive Smart Structures and Integrated Systems XVII,
edited by Jinkyu Yang, Proc. of SPIE Vol. 12483, 124831K
 · 0277-786X · doi: 10.1117/12.2658471

of conventional actuators poses difficulty in their incorporation into medical imaging devices. The need for lighter, cost-effective actuators based on a novel driving principle has risen to address the problem. The current research has deployed shape memory alloy as the actuation element of the system. The SMA has been selected over other smart materials because of its high power/weight ratio and the high transformation strain. Thus, by using SMA, the development of a high-force/torque and high-stroke/angular displacement actuator could be envisaged.

In the open literature, researchers have reported the various design and development of SMA-based rotary actuators. One of the early development in the field of rotary actuators was sheet-based rotor[4] and box-type rotor,[5] which were able to generate a torque of 0.226 N-m and 0.21 N-m respectively. Subsequently, other rotary actuators were built to receive high angular displacement from the SMA-based actuation elements. In this work, a rotary differential SMA actuator based on the friction clutch mechanism was developed, generating high angular displacement up to the range of 30°.[6] Similarly, a rotary actuator based on a ball and screw was developed, which gave an angular displacement of up to 100°; however, the torque output was low in magnitude.[7] In the last decade, SMA-based rotary actuators were built with high angular displacement,[8] high rotational speed,[9] and compact design.[10] Similarly, other rotary actuators were developed that either focused on high angular displacement[11] or high rotational speed;[12] however, all of them had a torque output below 1.25 N-m. The maximum torque reported in the open literature via SMA-based rotary actuators was by the amagnetic SMA rotary actuator, which generated a torque of 1.2 N-m.[13] To address the challenge of low torque SMA-based actuators, the present study presents a novel ergonomic-design-integration-framework of a bioinspired SMA-driven rotary actuator capable of producing medium to high range torque and large angular displacement. The current study has integrated SMA springs into the system in a bipennate configuration. Hitherto, this arrangement has been used for developing a high-force linear actuator.[14] A total of sixteen springs (eight bipennate units) were incorporated and were able to generate a force of 136 N. Consequently, the developed novel rotary actuator generated a maximum torque of 2.1 N-m with a maximum angular displacement of 64°.

2. METHODOLOGY

2.1 Governing equations

The Shape Memory Alloy springs deployed in the rotary actuator showcase the shape memory effect (SME). The characteristics of SME can be best elucidated by going through the complex thermomechanical loading path where the strain undergone by the spring is a combination of the stress applied as well as the temperature of the spring. Initially, the spring is under no external loading and low temperature (below martensite finish temperature, M_f), and the spring is in the twinned martensite phase (M^t). On further loading, beyond crossing a certain threshold stress (detwinning finish stress, σ_f), the spring transforms to the second martensitic variant via the shear lattice distortion, detwinned or reoriented martensite (M^d). Subsequent heating of the spring commences the reverse transformation when it crosses the austenite start temperature (A_s) and completes at austenite finish temperature (A_f). The strain retrieved from the transformation is called the transformation strain (ϵ_t). Ensuring the cooling of the SMA springs results in the forward transformation, which initiates at the martensite start temperature (M_s) and completes at the martensite finish temperature (M_f). This is the one-way SME and the cycle of which can be repeated multiple times.

Hence, to explain the shape memory behavior of SMA, which relies on thermo-mechanical characteristics and changes in macroscopic crystal structure related to phase transitions, several researchers have suggested an array of approaches. The model proposed by Tanaka,[15] which assumes the martensite volume fraction is related to the temperature and stress as an exponential function, has been most widely used for engineering applications. Subsequent to that, Liang and Rodgers,[16] and Brinson[17] proposed an alternative model where the phenomenological model was a function of the cosine of temperature and stress. Bekker and Brinson[18] suggested a phase diagram-based kinetic model describing the behavior of SMA material under various loading circumstances and partial transformation. Banerjee[19] used the Bekker and Brinson[18] phase diagram-based kinetics technique to simulate the Elahinia and Ahmadian[20] single degree of freedom manipulator. For engineering applications, it is challenging to execute the phase diagram-based kinetics method that considers a non-monotonic change of stress with temperature. Elahinia and Ahmadian[21] addressed these flaws in the pre-existing phenomenological

models and provided an improved phenomenological model to analyze and evaluate the shape memory behavior under any complicated loading situations.

The SMA coil (spring) modeling, however, is more intricate than straightforward wire modeling. Although the tension on a wire is uniformly distributed over its whole cross section, on a spring, the stress monotonically rises from the wire's centre to its periphery. This occurs because the axially applied force is converted to a torsional moment, and the shear stress is a function of the radius of the spring wire. This study, nonetheless, considers the maximum stress and strain of the periphery for analytical modeling and computation. Moreover, for the holistic modeling of the entire rotary actuator, the kinematics of the mechanism also needs to be taken into account. On heating the SMA spring, the springs start contracting as and when the temperature of the spring crosses the austenite start (A_s) temperature. As mentioned, the springs are arranged in a bipennate configuration, with one end fixed while the other is constrained to move along an axis. It is the free end that is connected to the follower, which on the contraction of SMA springs, moves along the axis and rotates the cam resulting in angular displacement and torque.

2.1.1 SMA coil (spring) model for large deformation

In the case of large SMA spring deformation, the change in the pitch angle of the coil as well as the spring diameter is significant and cannot be considered negligible. The same is the case with the torque and the bending moment. However, the coil spring curvature effect has not been considered in the analytical computation. The relation between the axial force and the large deflection is given by,[22,23]

$$x = -\frac{8nD_f^3}{d^4 \cos\alpha_f}\left(\frac{\cos^2\alpha_f}{G} + \frac{2\sin^2\alpha_f}{E}\right)F \tag{1}$$

where G is the phase-dependent shear modulus of SMA and is obtained using $G = \xi G_M + (1-\xi)G_A$, G_A and G_M represents the shear modulus of austenite and martensite phase respectively. Meanwhile, the D_i and D_f denote the initial and final spring diameter, respectively, while α_i and α_f denote the initial and final pitch angle, respectively, where $D_f = D_i(\cos\alpha_f/\cos\alpha_i)$.

It is imperative to note that the deflection term consists of two separate terms. While the former is the torque-related term the latter is related to the bending moment. It can be inferred from the trigonometric coefficients present in each term that the ratio of torque to bending moment term reduces with increasing pitch angle (α). It is also imperative to note that the shape memory alloy spring is considered to be isotropic, and hence shear modulus (G) can be written as $E/2(1+\nu)$.

The length of the spring, as illustrated in Figure 1b, is a function of n (number of coils), α (pitch angle), D (diameter of the SMA spring), and d (diameter of the spring wire). The length of the spring thus can be represented by,

$$L = n \cdot (\pi D \tan\alpha + d) \tag{2}$$

Additionally, the deflection (x) can also be written in terms of the change in length,

$$x = L_i - L_f \tag{3}$$

$$x = \frac{n\pi D_i}{\cos\alpha_i}(\sin\alpha_i - \sin\alpha_f) \tag{4}$$

Equation 3 can be simplified further to relate the pitch angle with respect to the deflection (x),

$$\alpha_f = \cos^{-1}\sqrt{1 - \left(\sin\alpha_i - \frac{x\cos\alpha_i}{\pi n D_i}\right)^2} \tag{5}$$

While the geometric constraint has been established, it is essential to establish the relationship between the axial force and shear stress developed in the spring. Therefore, to begin with, with the axial force being applied at the center, the shear stress has been derived under the assumption that the torque moment is a resultant of the entire force and is given as,

$$\tau = \frac{8D_f}{\pi d^3} F \tag{6}$$

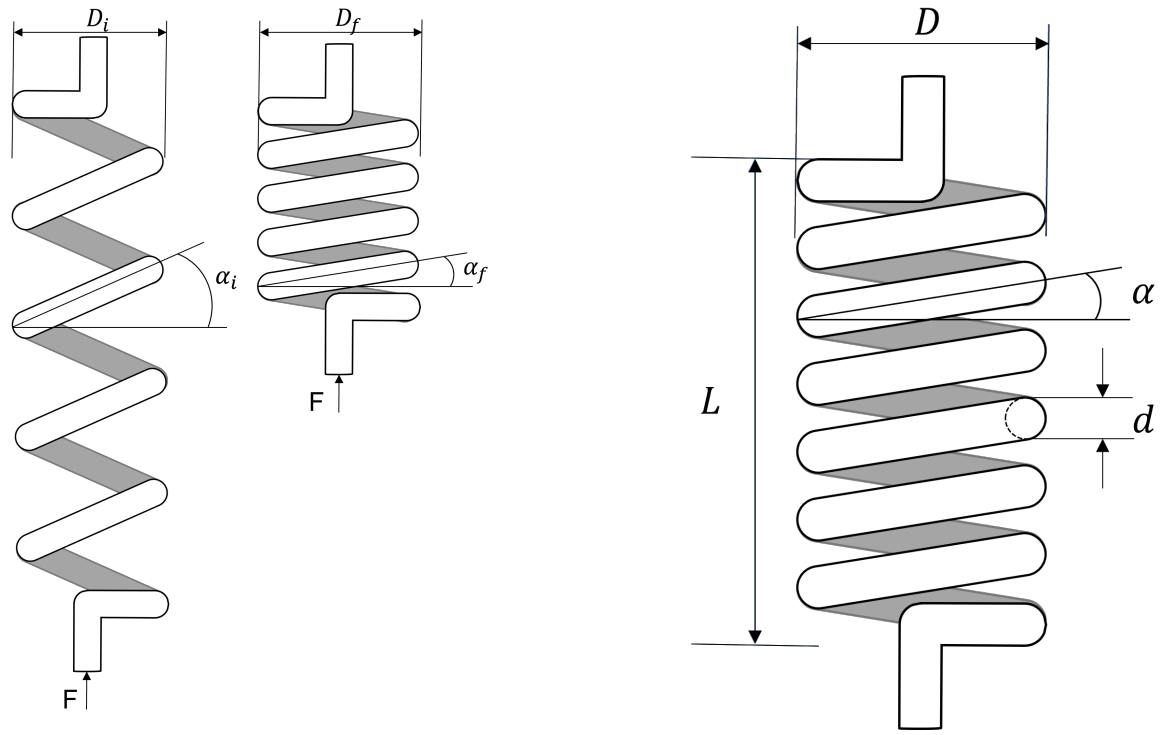

(a) (b)

Figure 1: The figure illustrates the various important geometric parameters that have been taken into consideration while analytically modeling the spring, (a) depicts the two distinct stages of SMA spring contraction. The left image denotes the initial stage of the spring where α_i and D_i denotes the initial spring pitch angle and the spring initial diameter, respectively. The right image shows the final condition of the spring where α_f and D_f represent the final spring pitch angle and the spring final diameter, respectively, (b) the figure shows the length of the spring and is given by $L = n(\pi D \tan\alpha + d)$, where n denotes the number of coils.

As the relationship between shear stress and the axial force has been established, it is essential for the analytical modeling to analyze the shear strain as well as the deflection of the spring with respect to the shear stress produced. To begin with, the deflection relationship can be found out by substituting Equation 6 into Equation 1 to get,

$$x = -\frac{n\pi D_i^2 \cos\alpha_f}{Gd\cos\alpha_i^2}\left(\frac{1+\nu\cos^2\alpha_f}{1+\nu}\right)\tau \tag{7}$$

And $\dot{x}$ can be easily derived by taking the time derivative of Equation 7 to get,

$$\dot{x} = -\frac{n\pi D_i^2}{d(1+\nu)\cos\alpha_i^2}\left[\frac{\dot{\tau}G - \dot{G}\tau}{G^2}\left[\cos\alpha_f(1+\nu\cos^2\alpha_f)\right] + \frac{\tau}{G}(1+\nu\cos^2\alpha_f)\frac{d}{dt}\cos\alpha_f + 2\nu\cos\alpha_f^2\left(\frac{\tau}{G}\right)\frac{d}{dt}\cos\alpha_f\right)\right] \quad (8)$$

The value of shear strain γ can be obtained by getting the form $\tau = G\gamma$. This form can be obtained by rearranging the Equation 7 and substituting the value of x from Equation 4 to get,

$$\gamma = \frac{\tau}{G} = \frac{d(1+\nu)\cos\alpha_i(\sin\alpha_f - \sin\alpha_i)}{D_i\cos\alpha_f(1+\nu\cos^2\alpha_f)} \quad (9)$$

2.1.2 Constitutive modeling

The constitutive equation helps identify the dynamics of the SMA spring by relating the shear stress to the shear strain, martensite Volume fraction, and the temperature of the spring. Liang and Rogers[16] established a one-dimensional relationship between shear stress and shear strain. It was Hyo Jik Lee,[24] and Hao Liu[25] who proposed a modified shear stress and strain model. The shear strain-shear stress relationship is expressed by,

$$\tau - \tau_i = G(\gamma - \gamma_i) + \Omega(\xi - \xi_i) + \frac{\theta_T}{\sqrt{3}}(T - T_i) \quad (10)$$

where, G is the shear modulus of SMA which is a function of martensite volume fraction (ξ), is obtained using $G = \xi G_M + (1-\xi)G_A$, G_A and G_M depicts the shear modulus of austenite and martensite phase respectively, while the thermal elastic coefficient is represented by θ_T. The shear transformation constant Ω is represented by $\Omega = -\gamma_L G$, γ_L referring to the maximum residual strain. The subscript i denotes the initial conditions.

2.1.3 Phase transformation equation

Since most of the properties of SMA as well as the shear stress is a function of martensite volume fraction, it is imperative to get the value of martensite volume fraction. As mentioned earlier, the phase transformation model presented here is the enhanced phenomenological model propounded by Elahinia and Ahmadian.[21] The current model captures the dependency of martensite volume fraction on temperature and shear stress.

- **Reverse transformation (martensite to austenite)**

  The transformation of SMA from martensite to austenite (reverse transformation) through heating is described by the governing equation:

  $$\xi = \frac{\xi_0}{2}\left[\cos\left[a_A\left(T - A_s\right) + b_A\tau\right] + 1\right] \quad (11)$$

  where, ξ denotes the martensite volume fraction, ξ_0 is the initial martensite volume fraction before commencing the heating cycle, $a_A = \pi/(A_f - A_s)$, $b_A = -a_A/C_A$ and C_A are curve-fitting parameters, T is the temperature of the spring, A_s and A_f are the temperatures where the martensite start converting to austenite (austenite start temperature) and the complete transformation to austenite occurs (austenite finish temperature), respectively.

- **Forward transformation (austenite to martensite)**

  The transformation of SMA from austenite to martensite (forward transformation) through cooling is described by the governing equation:

  $$\xi = \frac{1-\xi_0}{2}\cos\left[a_M\left(T - M_f\right) + b_M\tau\right] + \frac{1+\xi_0}{2} \quad (12)$$

where, ξ_0 is the initial martensite volume fraction before commencing the cooling cycle, $a_M = \pi/(M_s - M_f)$, $b_M = -a_M/C_M$ and C_M are curve-fitting parameters, T is the temperature of the spring, M_s and M_f are the temperatures where the austenite start converting to martensite (martensite start temperature), and the complete transformation to martensite occurs (martensite finish temperature), respectively.

The rate of change of ξ, upon differentiating Equation 11 and 12, is guided by:

$$\dot{\xi} = \eta_\tau \dot{\tau} + \eta_T \dot{T} \tag{13}$$

where, the values of coefficients (η_τ and η_T) differ in cooling and heating stage.

2.1.4 Heat transfer equation

As mentioned, SMA actuates when the temperature of the wire crosses a certain transition temperature. The temperature of the spring is elevated via resistive heating (Joule heating). The temperature of the spring is dependent on three terms, the current passing through the spring, the convective heat loss, and the latent heat of transformation during the phase change. Thus, the energy balance equation is given by:

$$m_{spring} c_p \dot{T} = \frac{I_{in}^2 l}{A_{cross}} [\xi \rho_M + (1 - \xi)\rho_A] - A_c h_T (T - T_\infty) + m_{spring} \Delta H \dot{\xi} \tag{14}$$

where, m_{spring} denotes the total mass of SMA spring, c_p is the specific heat capacity of the SMA, I_{in} is the current passed through the spring, $(l/A_{cross})[\xi\rho_M + (1-\xi)\rho_A]$ is the ohmic resistance of the SMA spring, with ρ_M and ρ_A is the resistivity of the SMA spring in martensite and austenite phases, respectively. While A_c is the curved surface area of the SMA spring, A_{cross} is the cross-section area of the spring wire, ΔH is the latent heat of transformation of the SMA spring, T_∞ represent the temperature of the environment.

2.1.5 Follower displacement - SMA spring deflection equation

The springs are arranged in a bipennate configuration where the springs are inclined obliquely (angle of pennation) to the shaft attached to the follower. While one end of the spring is fixed, the movable end is attached to the shaft, which in turn is constrained to move in a straight line. On increasing the temperature of the wire through resistive heating, the SMA spring contracts; however, the spring deflection experienced by the spring as mentioned in Equation 4 is not equal to the deflection of the shaft (follower) because of the angle of pennation (α^{penn}). Hence the follower deflection is related to the spring deflection by,

$$x_{follower} = L_i \cos \alpha_i^{penn} - (L_i - x) \cos \alpha^{penn} \tag{15}$$

where, $x_{follower}$ is the deflection of the follower, L_i is the initial length of the spring, α_i^{penn} is the initial pennation angle and α^{penn} is the pennation angle at a time t.

2.1.6 Torque dynamics equation

The distance of any point on the cam can be written in terms of θ (the angle formed between the line joining the center of the cam and the point of contact and the major axis) as,

$$R = \frac{ab}{\sqrt{a^2 \sin^2 \theta + b^2 \cos^2 \theta}} \tag{16}$$

where, a is the semi-major axis, and b is the semi-minor axis of the cam, while θ is the angle formed between the line joining the center of the cam and the point of contact and the major axis.

α, on the other hand, is the angle formed between the tangent drawn at the point of contact (x_0, y_0) and the positive direction of the major axis and is depicted by:

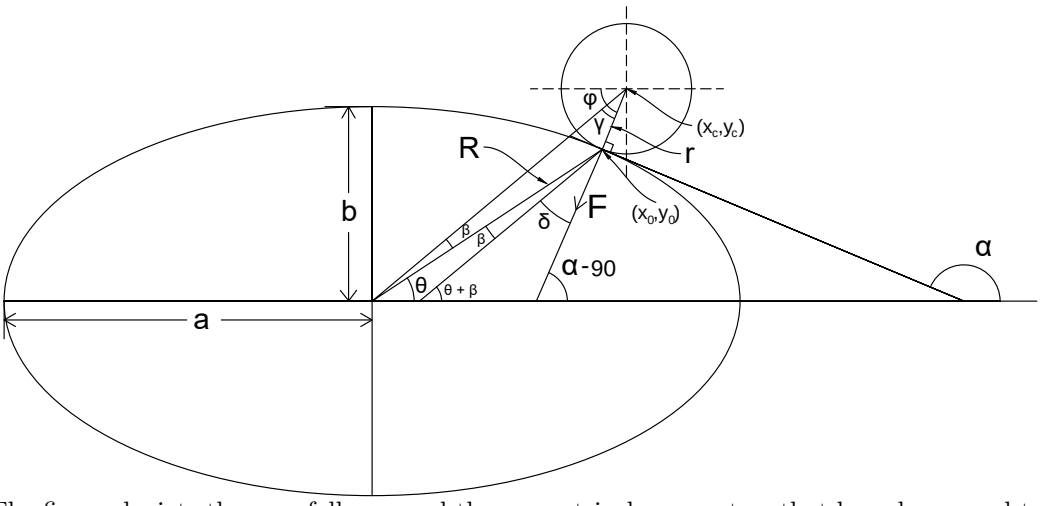

Figure 2: The figure depicts the cam follower and the geometrical parameters that have been used to model the torque. The ellipse depicts the cam profile, while the smaller circle of radius r denotes the follower. The cam has a semi-major axis a and a semi-minor axis of b, and the distance from the center of the cam to the point of contact of the cam and follower (x_0, y_0) is represented by R. The angle subtended by the line joining the center of the cam and the center of the follower and the line joining the center of the cam and point of contact (x_0, y_0) is β. The angle θ is the angle formed between the line joining the center of the cam and the point of contact and the major axis.

$$\alpha = \tan^{-1}\left(-\frac{b^2}{a^2}\cot\theta\right) \tag{17}$$

After solving the geometrical constraints, as illustrated in Figure 2, the torque generated at the center due to the force transmitted by the follower is given by,

$$\Gamma = -FR\cos(\alpha - \theta) \tag{18}$$

Substituting Equation 17 into Equation 18 we get torque solely as a function of θ,

$$\Gamma = -FR\cos\left[\tan^{-1}\left(-\frac{b^2}{a^2}\cot\theta\right) - \theta\right] \tag{19}$$

It is imperative to note that the angular displacement found experimentally is $\theta + \beta$ and torque is dependent on θ and hence, it is important to find the value of θ from $\theta + \beta$. The same is formulated geometrically to get,

$$\tan(\theta + \beta) = \frac{R\sin\theta - r\cos(\tan^{-1}[-(b^2/a^2)\cot\theta])}{R\cos\theta + r\sin(\tan^{-1}[-(b^2/a^2)\cot\theta])} \tag{20}$$

where R is the radius of the cam while r denotes the radius of the follower. The equation has been solved numerically using the Newton-Rhapson method.

On heating the SMA spring, the temperature of the spring increases and it contracts. When the spring is contracted, a percentage of the spring deflection x is witnessed in the follower $x_{follower}$. The displacement of the follower $x_{follower}$ and the force transmitted by the follower F, results in torque T and angular displacement $\theta + \beta$. The angular displacement as a function of displacement of the follower $x_{follower}$ is depicted by,

$$a + r - \sqrt{R^2 + r^2 - 2Rr \sin\left[\theta - \tan^{-1}\left(-\frac{b^2}{a^2}\cot\theta\right)\right]} = x_{follower} \tag{21}$$

2.2 Concept and prototyping

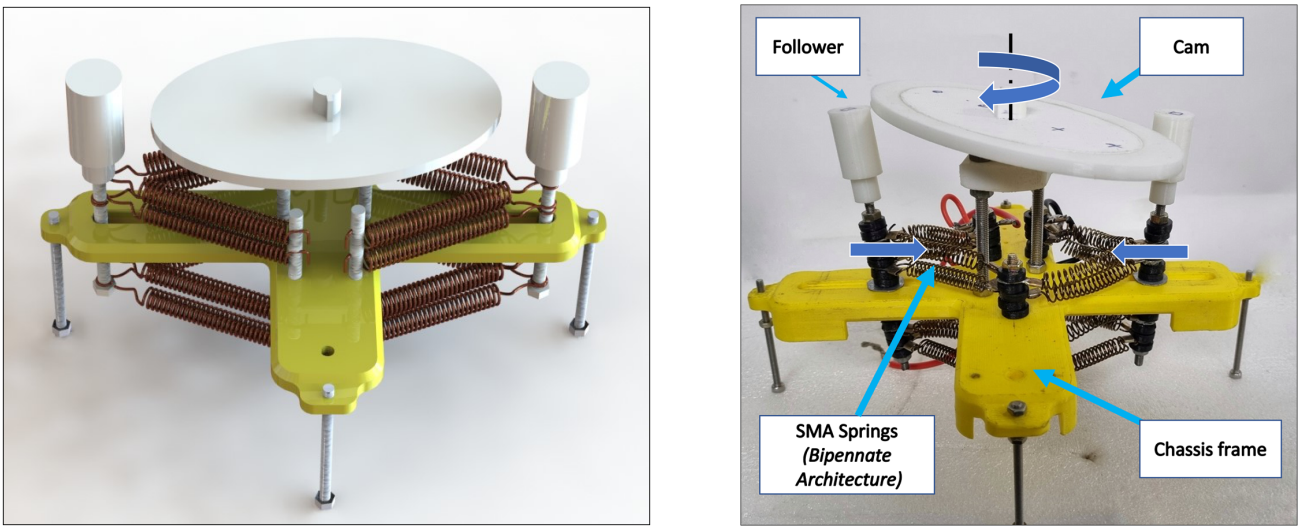

(a) (b)

Figure 3: The SMA-based rotary actuator where the SMA springs are arranged in a bipennate configuration, (a) CAD model of the prototype that has been 3-D printed, (b) depicts the developed rotary actuator prototype. The figure shows the SMA spring in an actuated stage, where the springs are close to the solid length. The direction of the rotation of the cam and the direction of the follower displacement has been illustrated.

An SMA-based rotary actuator prototype has been developed in an effort to validate the analytical results with the experimental data. The prototype was fabricated using additive manufacturing techniques, using Ultimaker 3 Extended 3D printer. The CAD model developed for 3-D printing has been shown in Figure 3a. In order to provide sturdiness to the body, the Polylactic acid (PLA) material is used for the 3D printing of the cam, follower, and chassis frame. However, the spacer (to separate two SMA springs) was built using Poly-Carbonate (PC) due to its heat-resilient property since the component is directly in contact with the heated stage of SMA springs. The SMA springs and their physical properties have been taken from *Dynalloy, Inc* for analytical computation. The angle subtended by the springs with the follower's path is the pennation angle (α^{penn}). While the movable end of the SMA spring is connected to the follower, the fixed end was fastened on the bolt (which was on the chassis frame) with the help of terminal crimps. A total of sixteen springs have been used in the rotary actuator, where four groups of four springs are electrically connected in parallel, while each spring in every group is in series. An insulating sleeve has been put over the bolt, as multiple springs are put on every bolt, and spacers have been put between each SMA springs to provide enough gap between the two adjacent springs to avoid short-circuiting. An input current of 16 A was provided as the source to increase the temperature of the wire via the Joule heating effect.

2.3 Experimentation

The experiments have been performed on the prototype developed, as shown in Figure 3b. A DC programmable power supply was used to actuate the entire actuator, where 16 A current was provided to the system during the actuation cycle of 10 sec. Meanwhile, PACEline CFT/5kN piezoelectric load cell was deployed to measure the blocked force generated by the bipennate spring, as shown in Figure 4a. Under the effect of Joule heating, the temperature of the SMA spring is increased, resulting in the contraction of the spring. Consequently, the

follower bolt displaces and touches the force transducer. The data logger is connected to the host computer, which is required for storing the blocked force data and post-processing.

Furthermore, the rotation angle is measured with the help of the overhead camera, as illustrated in Figure 4c. During actuation, the SMA springs start to contract because of the shape memory effect. Since the free end of the spring is fixed on the follower, the path of which is guided by a slot, the followers move in the direction as shown in Figure 3b. Consequently, due to the movement of the followers, the cam rotates, which is captured by the overhead camera. The recorded video is fed as an input in the bounding box algorithm, which follows the patterns (◯, ×, and □) drawn on the cam and follower. The angle of the follower is considered as the datum, and the angle of the rotation is measured with respect to the datum.

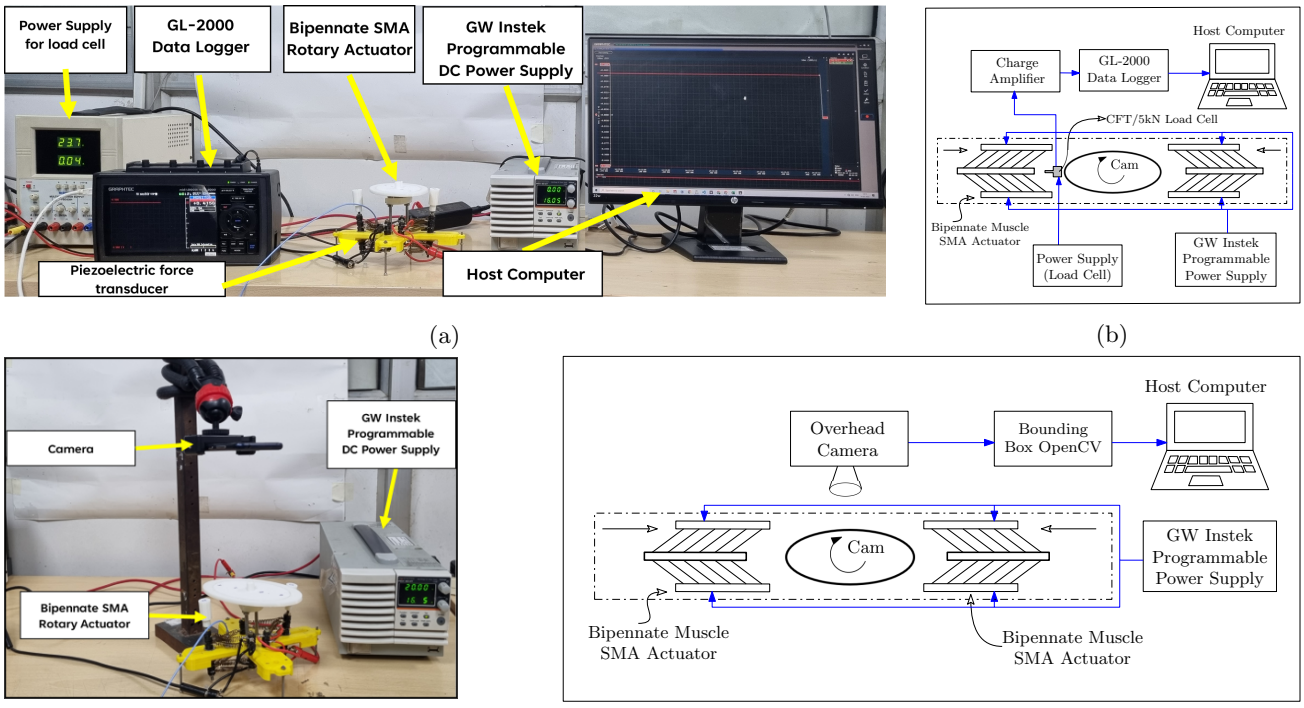

Figure 4: (a) The experimental setup for measuring the force generated by the bipennate SMA springs. A constant 24 V power supply has been used to power the Piezoelectric load cell. The GW Instek programmable DC power source was used to provide 16 A current to the rotary actuator. Also, the force transducer is connected to the GL-2000 data logger, which is connected to the host computer, (b) the experimental setup schematic for measuring the force, (c) the experimental setup for measuring the angle of rotation of the cam. The rotary actuator was powered by the DC programmable supply. An overhead camera was fixed on top of the rotary actuator, which records the video. The video is then sent to the Host Computer, which uses a bounding box algorithm to find the rotation angle, and (d) the experimental setup schematic for measuring the angular displacment.

3. RESULTS AND DISCUSSION

The prototype illustrated in the Figure 3b has been experimentally tested, and the aforementioned Equations (1) - (21) have been used for analytical study. In the case of experimental analysis, the force generated by the SMA spring arranged in a bipennate configuration has been recorded. It is imperative to note that the force transmitted to the cam for rotation (responsible for generating torque at the center) will be a component of the force generated by the SMA spring. Furthermore, the angular displacement of the cam has been measured via the bounding box algorithm. A differential voltage has been established to increase the temperature of the wire beyond the phase transition temperature. An input current of 16 A has been provided as an input to the

overall circuit, resulting in a current of 4 A across each SMA spring. Additionally, a piezoelectric load cell was deployed to record the force transmitted by the bipennate spring, and an overhead camera was used to measure the angular displacement of the cam.

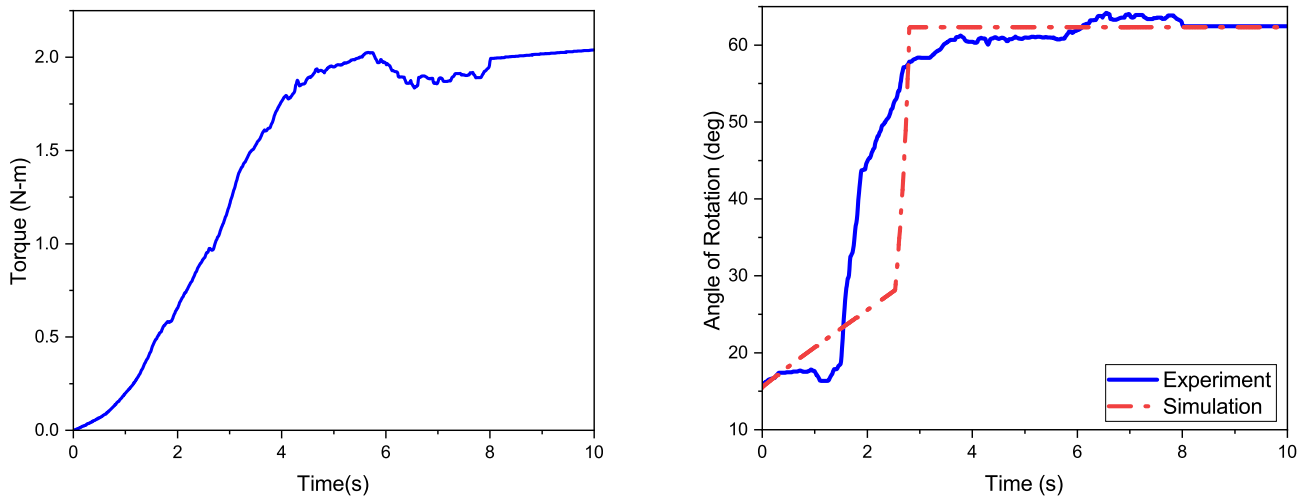

(a) (b)

Figure 5: The figure illustrates the torque obtained from experimental analysis and the validation of the analytical model using the experiments, (a) depicts the torque obtained via the bipennate-based SMA rotary actuator. A maximum torque of 2.1 N-m was generated, (b) depicts the validation of the analytical model developed for the rotary actuator. The angle of rotation of the cam has been compared for the same timeframe. A good agreement has been found between the analytical model and experimental results.

The torque obtained is a function of both the force transmitted by the bipennate-based SMA spring and the angle of rotation of the cam. From Equation 19, it can be inferred that the torque at a constant force gradually increases, reaches a maximum, and then starts decreasing with respect to the angle of rotation. Since the force is monotonically increasing, the effect of the angle parameter is overcome by the increasing force, and hence, the torque is continuously increasing to generate a maximum torque of 2.1 N-m in the 10 sec actuation cycle, as shown in Figure 5a. Furthermore, the angle of rotation is used to validate the analytical model with respect to the experimental data. An input current of 4 A for 10 sec has been considered during the actuation cycle both in analytical as well as experimental studies. The SMA spring was modeled using Equations (1) - (14), and the deflection of the spring x was obtained. With the help of geometric constraint, the deflection is then used to find the deflection of the follower $x_{follower}$, as shown in Equation 15. Further, the $x_{follower}$ obtained is then used to find the angle of rotation using Equation 20 and 21. As depicted in Figure 5b, a good agreement is found between the analytical and experimental results, where the maximum angular displacement found by experimental results and analytical model are 64° and 62° respectively.

For the blocked force measurement, a PACEline CFT/5kN piezoelectric force transducer has been used, as shown in Figure 4a. In total, sixteen springs have been used in the experiment where four groups of four SMA springs have been made, where each spring in every group is electrically connected in series, while all the groups are connected in parallel. A total of 16 A of input current was supplied, with each SMA spring being supplied a current of 4 A. The piezoelectric force transducer is placed in the path of the follower, and the blocked force is subsequently measured. The SMA springs arranged in a bipennate configuration produce a monotonically increasing force, as illustrated in Figure 6a, and the maximum force generated was 136 N during the actuation cycle. Meanwhile, the angle of rotation, as depicted in Figure 4d, was measured using the bounding box algorithm. An overhead camera was set up, and the video recorded through that was fed as an input to the bounding box algorithm. Furthermore, different shapes (◯, ×, and □) were drawn at opposite corners of the major axis of the cam and at the center of the two followers. The follower angle was considered as the datum point, and the angle of rotation of the cam was measured with respect to the follower angle using the OpenCV

library. The maximum angle of rotation from the rotary actuator was 64° as shown in the Figure 6b.

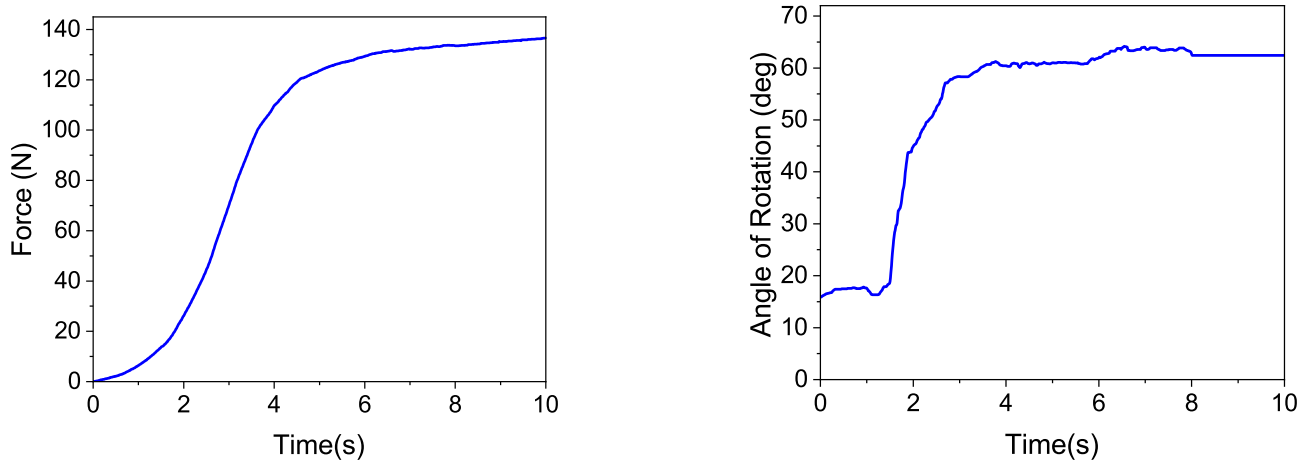

(a) (b)

Figure 6: The plot depicts both the force generated by the SMA spring as well as the angular displacement of the cam, (a) the SMA spring blocked force was measured via a piezoelectric force transducer. The force is monotonically increasing in nature and achieves a maximum of 136 N with 16 SMA springs arranged in bipennate configuration, (b) the angle of rotation was measured with the help of the overhead camera, and the maximum angular displacement achieved was 64°.

As mentioned in Equation 20, the angle measured via the experiment was $\theta + \beta$. Thus, it is imperative to find out the value of θ from $\theta + \beta$, as θ governs the distance from the center of the cam and the point of contact between the cam and follower and hence, the torque generated, as shown in Equation 16 and 19. θ is the angle formed between the line joining the center of the cam and the point of contact of the cam and follower and the major axis of the cam. β, on the other hand, is the angle formed between the line joining the center of the cam and the point of contact of the cam and follower and the line joining the center of the cam and the center of the follower. Applying the Newton-Rhapson method and using Equation 20, θ has been calculated from $\theta + \beta$ data. As depicted in Figure 7c, the value of β increases gradually and then starts decreasing; however, the β is lesser in magnitude (the maximum value attained was 4°). Hence, the trend and value of θ largely impact and dictate the characteristic and magnitude of $\theta + \beta$. While the maximum value of θ was found to be 61°, as shown in Figure 7b, the maximum value of $\theta + \beta$ was to be 64°, as illustrated in Figure 7a.

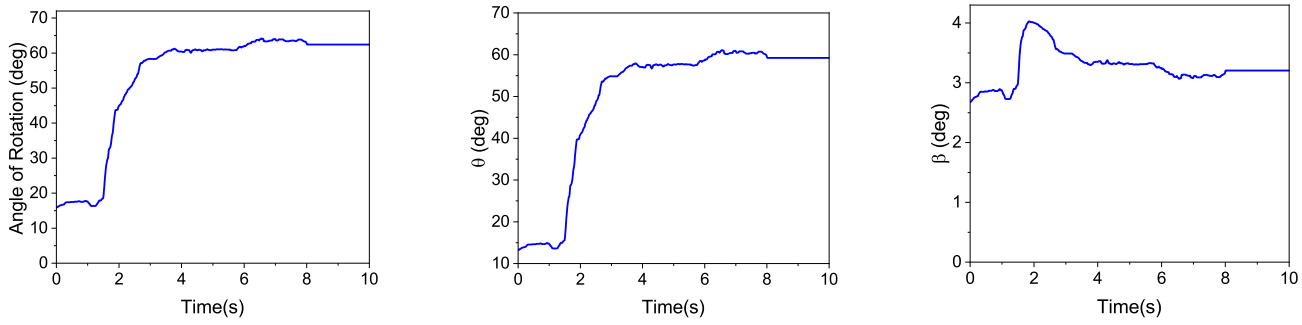

(a) (b) (c)

Figure 7: The figure depicts the three different angles that have been used in the experimental and analytical modeling, (a) depicts the angle of rotation of the cam and is given $\theta+\beta$. This is the angle that has been measured using experimentation, (b) shows the temporal variation of θ. The value of $\theta + \beta$ is dictated by θ, (c) shows the temporal variation of β. The value of β increases with the angular displacement of the cam to reach a maximum and then decreases.

4. CONCLUSION

A novel ergonomic-design-integration-framework of a bioinspired SMA-driven rotary actuator producing medium-to-high torque along with high angular displacement has been presented in the current study. The current study exploits the advantages of bipennate muscle architecture in the human body, as the SMA springs are arranged in the selfsame manner. The bipennate architecture results in generating a high force in a limited space. Subsequently, an analytical model of the rotary SMA actuator was developed comprising the dynamics of SMA along with the cam follower mechanism. The entire analytical simulation was performed on MATLAB R2020b and Simulink. Meanwhile, the prototype developed for experimental analysis was fabricated using additive manufacturing techniques. An experimental analysis of the torque generated and the angular displacement was performed on the prototype developed. The experimental result was highly consistent with the results obtained from the mathematical model, validating the physics developed for the entire Bipennate SMA-based rotary actuator.

The current research was carried out to develop an alternative solution to the conventional actuation system and overcome shortcomings suffered by such actuators. The novel driving principle of the rotary actuator presented in this study makes it easier to integrate it into devices where the electromagnetism-based actuator is found to be a hindrance. One such example would be medical imaging devices, such as Magnetic Resonance Imaging, as it is quite susceptible to the noises created due to electromagnetism. Furthermore, the actuator can incorporate a compliant-stroke-amplification mechanism to improve further the angular displacement achieved by the current rotary actuator. The application of this actuator can be found in healthcare actuators and mobile robotics as well.

ACKNOWLEDGMENTS

This research work has been funded by Portescap India Pvt. Ltd. through a Corporate Social Responsibility (CSR) grant (Project Number: PIPL/DORA/2020022). The authors thank Ratnangshu Das and Abhishek Kumar Singh, who provided insight and expertise that greatly assisted the research.

REFERENCES

[1] Carlson, B. M., "The muscular system," *The Human Body* , 111–136 (2019).

[2] Jenkins, T. and Bryant, M., "Pennate actuators: force, contraction and stiffness," *Bioinspiration & Biomimetics* **15**(4), 046005 (2020).

[3] Chaurasiya, K. L., Harsha, A. S., Sinha, Y., and Bhattacharya, B., "Design and development of non-magnetic hierarchical actuator powered by shape memory alloy based bipennate muscle," *Scientific Reports* **12**(1), 10758 (2022).

[4] Kuribayashi, K., "A new servo motor using shape memory alloy," in [*15th Annual Conference of IEEE Industrial Electronics Society*], 238–243, IEEE (1989).

[5] Tanaka, Y. and Yamada, A., "A rotary actuator using shape memory alloy for a robot-analysis of the response with load," in [*Proceedings IROS'91: IEEE/RSJ International Workshop on Intelligent Robots and Systems' 91*], 1163–1168, IEEE (1991).

[6] Gorbet, R. B. and Russell, R. A., "A novel differential shape memory alloy actuator for position control," *Robotica* **13**(4), 423–430 (1995).

[7] Yuan, H., Fauroux, J.-C., Chapelle, F., and Balandraud, X., "A review of rotary actuators based on shape memory alloys," *Journal of Intelligent Material Systems and Structures* **28**(14), 1863–1885 (2017).

[8] Song, G., "Design and control of a nitinol wire actuated rotary servo," *Smart materials and Structures* **16**(5), 1796 (2007).

[9] Sharma, S., Nayak, M., and Dinesh, N., "Modelling, design and characterization of shape memory alloy-based poly phase motor," *Sensors and Actuators A: Physical* **147**(2), 583–592 (2008).

[10] Lan, C.-C., Wang, J.-H., and Fan, C.-H., "Optimal design of rotary manipulators using shape memory alloy wire actuated flexures," *Sensors and Actuators A: Physical* **153**(2), 258–266 (2009).

[11] Yuan, H., Balandraud, X., Fauroux, J., and Chapelle, F., "Compliant rotary actuator driven by shape memory alloy," in [*New Advances in Mechanisms, Mechanical Transmissions and Robotics: Proceedings of The Joint International Conference of the XII International Conference on Mechanisms and Mechanical Transmissions (MTM) and the XXIII International Conference on Robotics (Robotics' 16)*], 343–350, Springer (2017).

[12] Hwang, D. and Higuchi, T., "A rotary actuator using shape memory alloy (sma) wires," *IEEE/ASME Transactions on mechatronics* **19**(5), 1625–1635 (2013).

[13] Viscuso, S. and Pittaccio, S., "Design and implementation of a portable amagnetic shape memory rotary actuator," *Journal of intelligent material systems and structures* **24**(4), 454–472 (2013).

[14] Bhattacharya, B., Harsha, A. S., and Chaurasiya, K. L., "Bipennate muscle architecture-based shape memory alloy embedded hierarchical actuator." Indian Patent Number: 414106 (December 2022).

[15] Tanaka, K., "Thermomechanical sketch of shape memory effect," *Res Mechanica* **18**, 251 (1986).

[16] Liang, C. and Rogers, C. A., "One-dimensional thermomechanical constitutive relations for shape memory materials," *Journal of intelligent material systems and structures* **8**(4), 285–302 (1997).

[17] Brinson, L. C., "One-dimensional constitutive behavior of shape memory alloys: thermomechanical derivation with non-constant material functions and redefined martensite internal variable," *Journal of intelligent material systems and structures* **4**(2), 229–242 (1993).

[18] Bekker, A. and Brinson, L. C., "Temperature-induced phase transformation in a shape memory alloy: phase diagram based kinetics approach," *Journal of the Mechanics and Physics of Solids* **45**(6), 949–988 (1997).

[19] Banerjee, A., "Simulation of shape memory alloy wire actuator behavior under arbitrary thermo-mechanical loading," *Smart materials and structures* **21**(12), 125018 (2012).

[20] Elahinia, M. H. and Ahmadian, M., "An enhanced sma phenomenological model: I. the shortcomings of the existing models," *Smart materials and structures* **14**(6), 1297 (2005).

[21] Elahinia, M. H. and Ahmadian, M., "An enhanced sma phenomenological model: Ii. the experimental study," *Smart materials and structures* **14**(6), 1309 (2005).

[22] An, S.-M., Ryu, J., Cho, M., and Cho, K.-J., "Engineering design framework for a shape memory alloy coil spring actuator using a static two-state model," *Smart Materials and Structures* **21**(5), 055009 (2012).

[23] Shigley, J. and Mischke, C., "Mechanical springs," *Mechanical Engineering Design; McGraw-Hill: New York, NY, USA* , 590 (2001).

[24] Lee, H. J. and Lee, J. J., "Time delay control of a shape memory alloy actuator," *Smart Materials and Structures* **13**(1), 227 (2004).

[25] Liu, H., Fu, Y., Yan, Z., Wang, P., and Wang, S., "A dynamic model for the active catheter actuated by the shape memory alloy coil spring," in [*2009 International Conference on Mechatronics and Automation*], 1968–1973, IEEE (2009).